

# Heat jet approach for finite temperature atomic simulations of two-dimensional square lattice

Baiyili Liu and Shaoqiang Tang\*

*HEDPS, CAPT, and LTCS, College of Engineering, Peking University, Beijing 100871, P.R. China*

*(Received September 23, 2015, Revised December 19, 2015, Accepted December 23, 2015)*

**Abstract.** We propose a heat jet approach for a two-dimensional square lattice with nearest neighbouring harmonic interaction. First, we design a two-way matching boundary condition that linearly relates the displacement and velocity at atoms near the boundary, and a suitable input in terms of given incoming wave modes. Then a phonon representation for finite temperature lattice motion is adopted. The proposed approach is simple and compact. Numerical tests validate the effectiveness of the boundary condition in reflection suppression for outgoing waves. It maintains target temperature for the lattice, with expected kinetic energy distribution and heat flux. Moreover, its linear nature facilitates reliable finite temperature atomic simulations with a correct description for non-thermal motions.

**Keywords:** heat jet approach; atomic simulations; finite temperature; square lattice

---

## 1. Introduction

Atomic simulations have become an indispensable tool in physics, mechanics, nano-materials and engineering. Although the computing power keeps growing, in most real applications it is still not adequate for a complete atomic resolution of the physics. Moreover, even one can afford such numerical expenses, the ultimate goal of computational sciences is an understanding of the underlying system out of big data, rather than merely the production of such data by computers. Therefore, to properly characterize the physical problem, to correctly specify the mathematical settings, and to design appropriate algorithms become even more important than the early days when the computable system sizes were much smaller.

Finite temperature atomic simulations pose subtle issues in this regard, even for seemingly simple crystalline solids. On the one hand, statistical mechanics, particularly the non-equilibrium theory, is based on a probabilistic description of the underlying microscopic system. It faces substantial challenges when we really delve into a microscopic sublattice, namely, when the number of atoms becomes moderate. In such a subsystem, even the definition of thermal physical quantities can be questionable. Nevertheless, one still borrows concepts emerged from large systems and clarifies the limitations and makes modifications, e.g., see (Lepri *et al.* 2003) and references therein. On the other hand, it is well known that many heat transport properties and

---

\*Corresponding author, Professor, E-mail: [maotang@pku.edu.cn](mailto:maotang@pku.edu.cn)

mechanical properties of solids depend on temperature. Hence, it is important to take thermal fluctuations and non-thermal motions into consideration simultaneously in atomic simulations.

To realize a heat-bath or thermostat for a lattice at target temperature, there are various methods, e.g., (Anderson *et al.* 1980, Berendsen *et al.* 1984, Nosé 1984 and Hoover 1985). The most popular ways include deterministic e.g., (Nosé 1984 and Hoover 1985) and Langevin stochastic heat bath (Bussi and Parrinello 2007, Dhar 2008). A Nosé-Hoover heat bath imposes a nonlinear feed-back to the atomic system after evaluating the deviation of the system average kinetic energy from the target temperature. A Langevin stochastic heat bath takes a delicate balance between random force and damping according to the fluctuation-dissipation theorem. One either connects all atoms with a heat bath, or several atoms near the boundaries with it. For the former, a non-thermal motion in a finite temperature simulation is accounted in the system kinetic energy. This leads to an overestimated transient temperature, and consequently an over-damping for the non-thermal motion. We remark that when the thermal fluctuations dominate and the system size is big enough, such overestimation and over-damping may be ignored. For the latter, the overestimation of temperature and over-damping for non-thermal motion do not occur. However, when the non-thermal motion propagates towards the boundaries, it is likely reflected back, unless special treatments are designed for the boundaries.

There are extensive works using the heat baths to explore thermal conduction in one-dimensional atomic chains with the FPU- $\beta$  potential (Lepri *et al.* 2003, Xiong *et al.* 2014), the Toda potential (Hatano 1999), the Frenkel-Kontorova potential (Ai and Hu 2011), the on-site potential (Giardinà *et al.* 2000), asymmetric potentials (Zhong *et al.* 2012, Savin and Kosevich 2014) and with mass disorder (Dhar 2008, Dhar *et al.* 2011), etc. In contrast, there are fewer results for two-dimensional lattices, due to computational costs and challenging numerical issues (Jackson and Mistriotis 1989, Lippi and Livi 2000, Yang *et al.* 2006, Xiong *et al.* 2010, Nishiguchi *et al.* 1992, Barik 2006, Yang 2002). Different from traditional heat baths, Karpov *et al.* proposed a phonon heat bath for harmonic chain and triangular lattice (Karpov *et al.* 2007). Without modifying the dynamic equations for interior atoms, they suggested to adopt a phonon representation for heat source and inject it via time history boundary condition. It allows non-thermal motions added on the thermal fluctuations. However, the time history kernel treatment is rather expensive, and therefore not practical for atomic simulations at finite temperature in general. We have proposed a heat jet approach for the one-dimensional atomic chain (Tang and Liu 2015). The main difference lies in the boundary treatment. We designed a linear two-way boundary condition that simultaneously suppresses reflection for outgoing waves and allows injection of incoming waves. The incoming waves maintain thermal fluctuations in the computational sub-chain, again in terms of a phonon representation. We demonstrated that this approach actually applies to weakly nonlinear chains, or at moderately high temperature.

In this paper, we extend the heat jet approach to the out-of-plane motion in a linear square lattice. Again the key issue is the design of an effective two-way boundary condition that fulfills reflection suppression and source wave injection. Then adopting a phonon representation for the source term, we realise a thermostat suitable for finite temperature atomic simulations.

In the rest of this paper, we first introduce the governing equations, and formulate a matching boundary condition. Based on this condition, we design a two-way boundary treatment. Heat source is then described. In Section 3, we discuss thermodynamics quantities in atomic settings. Numerical illustrations are then presented in Section 4. We make some concluding remarks in Section 5.

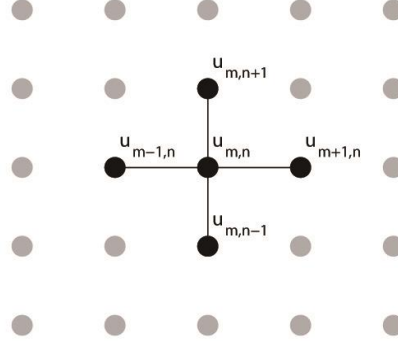


Fig. 1 Square lattice with nearest neighboring interaction

## 2. Formulation of heat jet approach for square lattice

In this section, we first describe the governing equation for a square lattice with harmonic interaction potential. Then we formulate a matching boundary condition that well suppresses spurious reflections, as well as incorporates wave inputs. With a heat source derived from a phonon representation of finite temperature atomic motion, we then obtain a close form of heat jet approach for atomic simulations at finite temperature.

### 2.1 Lattice dynamics model

We consider out-of-plane motion in an infinite square lattice of equal-mass atoms. See Fig. 1. Under nearest neighbouring interaction with harmonic potential  $V(r) = \frac{k}{2}r^2$ , the Hamiltonian is

$$H' = \sum_m \sum_n \left[ \frac{p_{m,n}^{\prime 2}}{2M} + V(u'_{m+1,n} - u'_{m,n}) + V(u'_{m,n+1} - u'_{m,n}) \right] \quad (1)$$

Here,  $M$  is the mass,  $k$  is the elastic constant,  $u'_{m,n}$  is the displacement of  $(m, n)$  atom away from its equilibrium position, and  $p'_{m,n} = M\dot{u}'_{m,n}$  is its momentum.

Let the lattice constant be  $a'$ . We define dimensionless quantities

$$a = 1, u_{m,n} = u'_{m,n} / a', t = t' / \sqrt{M/k}, p_{m,n} = p'_{m,n} / a' \sqrt{Mk}, H = H' / a'^2 k. \quad (2)$$

The rescaled Hamiltonian reads

$$H = \sum_m \sum_n \left[ \frac{p_{m,n}^2}{2} + V(u_{m+1,n} - u_{m,n}) + V(u_{m,n+1} - u_{m,n}) \right] \quad (3)$$

Accordingly, the non-dimensional Newton equation reads

$$\ddot{u}_{m,n} = u_{m+1,n} + u_{m-1,n} + u_{m,n+1} + u_{m,n-1} - 4u_{m,n}. \quad (4)$$

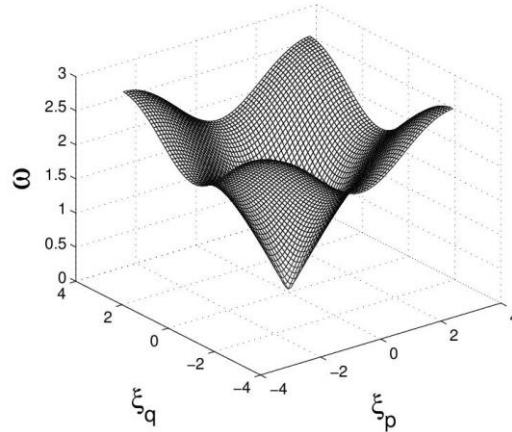


Fig. 2 Dispersion relation of the square lattice in the first Brillouin zone

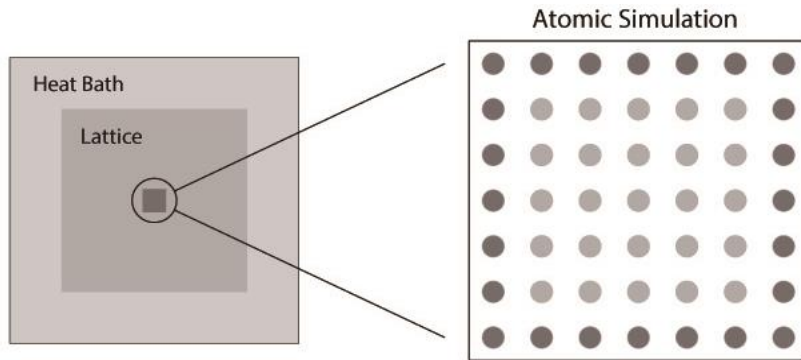


Fig. 3 Schematic plot of atomic simulations for square lattice

A monochromatic wave with wave vector  $(\xi_p, \xi_q)$  takes the form of  $u_{m,n} \sim e^{i(\omega t + \xi_p m + \xi_q n)}$ . Substituting this into the Newton equation, we find the dispersion relation

$$\omega(\xi_p, \xi_q) = 2\sqrt{\sin^2 \frac{\xi_p}{2} + \sin^2 \frac{\xi_q}{2}} \quad (5)$$

Due to periodicity, we restrict the wave vector  $(\xi_p, \xi_q)$  in the first Brillouin zone  $[-\pi, \pi] \times [-\pi, \pi]$ . See Fig. 2.

## 2.2 Matching boundary condition

To alleviate the immense load for computing the full atomic dynamics, one selects a much smaller domain for numerical simulations. This can be either an atomic simulation, or a multiscale simulation. The latter involves dynamical information exchange across the atomic scale and a coarse scale. At zero temperature, subdomain atomic simulations may often be performed with an artificial boundary treatment only, to avoid spurious reflections. In contrast, for a finite

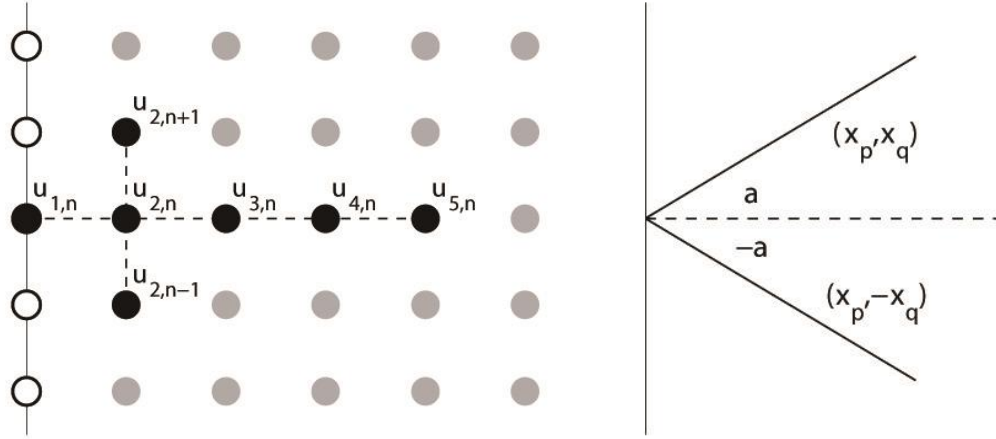


Fig. 4 Schematic plot of the left matching boundary condition

temperature simulation, thermal motion must be injected in a suitable way to maintain fluctuations in the interior domain. See Fig. 3. To be specific, we consider a rectangular computational domain containing  $N_x \times N_y$  atoms. We now design an accurate boundary treatment, which effectively suppresses spurious wave reflections for outgoing waves, meanwhile allows incoming waves being freely injected into the computational domain.

We start with a semi-infinite sub-lattice as the computational domain, namely,  $m > 1$  as shown in the left subplot of Fig. 4. We first assume all atoms in the rest domain ( $m \leq 0$ ) to be at equilibrium initially, and construct an artificial boundary condition to reproduce the correct dynamics inside the numerical subdomain. It amounts to make all outgoing waves passing through the numerical boundary without reflection. As one cannot afford the immense numerical cost for imposing an exact boundary condition in terms of the time history kernel treatment (Karpov *et al.* 2007, Pang and Tang 2011), we design instead an accurate boundary condition (Wang and Tang 2013), which is local in both space and time. In this way we considerably reduce the numerical cost while retain decent reflection suppression.

We discover by try and error that more atoms selected in the transverse direction helps absorbing incoming waves of high frequency. Meanwhile, adding atoms in the longitudinal direction helps absorbing incoming waves with large incident angle. Accordingly, we construct a matching boundary condition by relating the displacements and velocities near the boundary in a linear form.

$$\sum_{m=1}^5 c_{m,0} \dot{u}_{m,n} + c_{2,1} \dot{u}_{2,n+1} + c_{2,-1} \dot{u}_{2,n-1} - \sum_{m=1}^5 b_{m,0} u_{m,n} - b_{2,1} u_{2,n+1} - b_{2,-1} u_{2,n-1} = 0. \quad (6)$$

Considering the symmetry and linearity, we take  $c_{2,1} = c_{2,-1}$ ,  $b_{2,1} = b_{2,-1}$ , and  $c_{1,0} = 1$ .

Substituting the wave form  $u_{m,n} \sim e^{i(\omega t + \xi_p m + \xi_q n)}$  into Eq. (6) and discarding a common factor  $e^{i(\omega t + \xi_p m + \xi_q n)}$ , we define a matching residual function

$$\Delta(\xi_p, \xi_q) = i\omega(\xi_p, \xi_q) \left[ \sum_{m=1}^5 c_{m,0} e^{i\xi_p(m-1)} + c_{2,1} (e^{i(\xi_p+\xi_q)} + e^{i(\xi_p-\xi_q)}) \right] - \sum_{m=1}^5 b_{m,0} e^{i\xi_p(m-1)} - b_{2,1} (e^{i(\xi_p+\xi_q)} + e^{i(\xi_p-\xi_q)}). \tag{7}$$

For a normal incident wave with  $\xi_q=0$ , the matching residual function may be put as

$$\Delta(\xi_p, 0) = i\omega(\xi_p, 0) \left[ \sum_{m=1}^5 c_{m,0} e^{i\xi_p(m-1)} + 2c_{2,1} e^{i\xi_p} \right] - \sum_{m=1}^5 b_{m,0} e^{i\xi_p(m-1)} - 2b_{2,1} e^{i\xi_p}. \tag{8}$$

Noticing that  $i\omega(\xi_p) = i\xi_p + O(\xi_p^3)$ ,  $e^{i\xi_p} = 1 + i\xi_p + \frac{(i\xi_p)^2}{2} + O(\xi_p^3)$ , we perform Taylor expansions and require  $\Delta(\xi_p, 0) = o(\xi_p^2)$ . This yields the following algebraic equations.

$$-\sum_{m=1}^5 b_{m,0} - 2b_{2,1} = 0, \tag{9}$$

$$\sum_{m=1}^5 c_{m,0} + 2c_{2,1} - \sum_{m=1}^5 (m-1)b_{m,0} - 2b_{2,1} = 0, \tag{10}$$

$$\sum_{m=1}^5 (m-1)c_{m,0} + 2c_{2,1} - \sum_{m=1}^5 \frac{(m-1)^2}{2} b_{m,0} - b_{2,1} = 0. \tag{11}$$

Next, we may specify a certain wave vector  $(\xi_p^*, \xi_q^*)$  and require  $\Delta(\xi_p^*, \xi_q^*) = 0$ . This means transparent wave propagation across the boundary at such a wave vector, and mathematically leads to the following equations,

$$\sum_{m=1}^5 c_{m,0} \omega(\xi_p^*, \xi_q^*) \sin(\xi_p^*(m-1)) + c_{2,1} \omega(\xi_p^*, \xi_q^*) (\sin(\xi_p^* + \xi_q^*) + \sin(\xi_p^* - \xi_q^*)) + \sum_{m=1}^5 b_{m,0} \cos(\xi_p^*(m-1)) + b_{2,1} (\cos(\xi_p^* + \xi_q^*) + \cos(\xi_p^* - \xi_q^*)) = 0, \tag{12}$$

$$\sum_{m=1}^5 c_{m,0} \omega(\xi_p^*, \xi_q^*) \cos(\xi_p^*(m-1)) + c_{2,1} \omega(\xi_p^*, \xi_q^*) (\cos(\xi_p^* + \xi_q^*) + \cos(\xi_p^* - \xi_q^*)) - \sum_{m=1}^5 b_{m,0} \sin(\xi_p^*(m-1)) - b_{2,1} (\sin(\xi_p^* + \xi_q^*) + \sin(\xi_p^* - \xi_q^*)) = 0. \tag{13}$$

The choice of  $(\xi_p^*, \xi_q^*)$  in Eq. (12) and Eq. (13) determines the overall quality of the boundary condition. We select four vectors, namely, (0.5,0), (1.5,0), (0.5,0.5) and (1.5,1.5), as shown by solid triangles in Fig. 5.

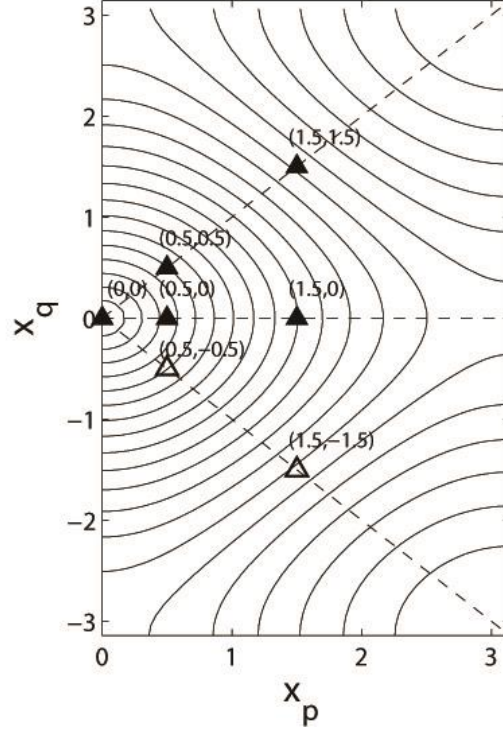


Fig. 5 The solid triangles represent wave vector  $(0, 0)$  for the long wave limit, and the selected wave vectors  $(\xi_p^*, \xi_q^*)$ . The curves are the contour lines for the dispersion relation

Solving the Eqs. (9)-(11) for the long wave limit, and Eqs. (12)-(13) for the four selected wave vectors, we get the following coefficients

$$\begin{aligned} c_{1,0} &= 1.0000, c_{2,0} = 3.3842, c_{3,0} = -5.7937, c_{4,0} = -0.0057, c_{5,0} = 0.5930, \\ c_{2,1} &= c_{2,-1} = 0.6733, \\ b_{1,0} &= -3.8274, b_{2,0} = 8.5111, b_{3,0} = 4.5064, b_{4,0} = -6.3485, b_{5,0} = 1.6292, \\ b_{2,1} &= b_{2,-1} = -2.2354. \end{aligned}$$

To check the quality for this set of parameters, we compute the reflection coefficient. Substituting the wave form  $u_{m,n} = e^{i(\omega t + \xi_p m + \xi_q n)} + R(\xi_p, \xi_q) e^{i(\omega t - \xi_p m + \xi_q n)}$  into Eq. (6), the reflection coefficient reads

$$R(\xi_p, \xi_q) = -\frac{\Delta(\xi_p, \xi_q)}{\Delta(-\xi_p, \xi_q)}. \quad (14)$$

As seen from Fig. 6, the proposed matching boundary condition suppresses reflections in a broad band, also effective for incoming waves with big wave number and large incident angle. The reflection coefficient is less than 1 over the whole right-half first Brillouin zone, indicating stability. We further remark that the symmetry consideration in taking  $c_{2,1} = c_{2,-1}$  and  $b_{2,1} = b_{2,-1}$

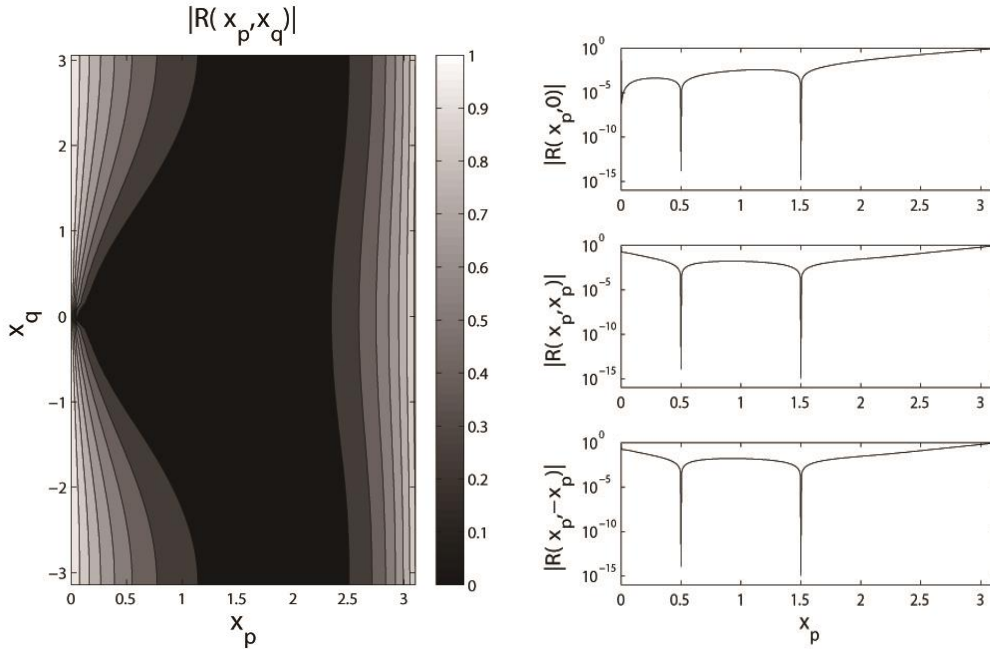


Fig. 6 Reflection coefficient of the matching boundary condition

leads to symmetric reflection suppression effects, as it is easy to show that  $R(\zeta_p, \zeta_q) = R(\zeta_p, -\zeta_q)$ . In another word, for waves at incident angles  $a$  and  $-a$ , the proposed matching boundary condition performs exactly the same. See the two lower right subplots of Fig. 6 for the reflection coefficient along  $\zeta_p = \zeta_q$  and  $\zeta_p = -\zeta_q$ . We further notice that extremely low reflection is reached at  $\zeta_p = 0.5, 1.5$ , as a consequence of our design for the boundary conditions.

We remark that the reflection coefficient is continuous with respect to the wave vector, except at the long wave limit. This is due to the fact that by our design  $\Delta(0,0) = 0$ , which makes the reflection coefficient being indefinite of the so-called  $0/0$  type. To circumvent the difficulty, we let  $(\zeta_p, \zeta_q) = (\zeta \cos a, \zeta \sin a)$ . Using the L'Hospital's rule for  $\zeta \rightarrow 0^+$ , we find that

$$\lim_{\zeta \rightarrow 0^+} R(\zeta \cos \alpha, \zeta \sin \alpha) = - \frac{\sum_{m=1}^5 c_{m,0} + 2c_{2,1} - \left( \sum_{m=1}^5 \cos \alpha (m-1) b_{m,0} + 2 \cos \alpha b_{2,1} \right)}{\sum_{m=1}^5 c_{m,0} + 2c_{2,1} + \left( \sum_{m=1}^5 \cos \alpha (m-1) b_{m,0} + 2 \cos \alpha b_{2,1} \right)}. \quad (15)$$

The dependency on the angle  $a$  may be observed from the different values of reflection coefficient in the right subplots of Fig. 6 at  $\zeta_p = 0$ . Actually it may be proved that for a normal incidence, in the long wave limit have different values as  $|R(\zeta_p, 0)|$  tends to 0, due to the requirement on coefficients in Eq. (10).

If a given incoming wave component  $w_{m,n}^{(1)}(t)$  is injected into the computational domain (Tang 2010), we apply the above matching boundary condition to the pure outgoing component  $u_{m,n}(t) - w_{m,n}^{(1)}(t)$ , and obtain

$$\begin{aligned} \dot{u}_{1,n} = & -c_{2,0}\dot{u}_{2,n} - c_{3,0}\dot{u}_{3,n} - c_{4,0}\dot{u}_{4,n} - c_{5,0}\dot{u}_{5,n} - c_{2,1}(\dot{u}_{2,n+1} + \dot{u}_{2,n-1}) \\ & + b_{1,0}u_{1,n} + b_{2,0}u_{2,n} + b_{3,0}u_{3,n} + b_{4,0}u_{4,n} + b_{5,0}u_{5,n} + b_{2,1}(u_{2,n+1} + u_{2,n-1}) + f_n^{(1)}(t). \end{aligned} \quad (16)$$

Here the source term is expressed in terms of  $w_{m,n}^{(1)}(t)$ ,

$$\begin{aligned} f_n^{(1)}(t) = & \dot{w}_{1,n}^{(1)} + c_{2,0}\dot{w}_{2,n}^{(1)} + c_{3,0}\dot{w}_{3,n}^{(1)} + c_{4,0}\dot{w}_{4,n}^{(1)} + c_{5,0}\dot{w}_{5,n}^{(1)} + c_{2,1}(\dot{w}_{2,n+1}^{(1)} + \dot{w}_{2,n-1}^{(1)}) \\ & - b_{1,0}w_{1,n}^{(1)} - b_{2,0}w_{2,n}^{(1)} - b_{3,0}w_{3,n}^{(1)} - b_{4,0}w_{4,n}^{(1)} - b_{5,0}w_{5,n}^{(1)} - b_{2,1}(w_{2,n+1}^{(1)} + w_{2,n-1}^{(1)}). \end{aligned} \quad (17)$$

In the same manner, we treat the other three boundaries. On the right boundary, we take

$$\begin{aligned} \dot{u}_{N_x,n} = & -\sum_{m=2}^5 c_{m,0}\dot{u}_{N_x+1-m,n} - c_{2,1}(\dot{u}_{N_x-1,n+1} + \dot{u}_{N_x-1,n-1}) \\ & + \sum_{m=1}^5 b_{m,0}u_{N_x+1-m,n} + b_{2,1}(u_{N_x-1,n+1} + u_{N_x-1,n-1}) + f_n^{(2)}(t), \end{aligned} \quad (18)$$

$$\begin{aligned} f_n^{(2)}(t) = & \sum_{m=1}^5 c_{m,0}\dot{w}_{N_x+1-m,n}^{(2)} + c_{2,1}(\dot{w}_{N_x-1,n+1}^{(2)} + \dot{w}_{N_x-1,n-1}^{(2)}) \\ & - \sum_{m=1}^5 b_{m,0}w_{N_x+1-m,n}^{(2)} - b_{2,1}(w_{N_x-1,n+1}^{(2)} + w_{N_x-1,n-1}^{(2)}). \end{aligned} \quad (19)$$

On the bottom boundary, we take

$$\begin{aligned} \dot{u}_{m,1} = & -\sum_{n=2}^5 c_{n,0}\dot{u}_{m,n} - c_{2,1}(\dot{u}_{m+1,2} + \dot{u}_{m-1,2}) \\ & + \sum_{n=1}^5 b_{n,0}u_{m,n} + b_{2,1}(u_{m+1,2} + u_{m-1,2}) + f_m^{(3)}(t), \end{aligned} \quad (20)$$

$$\begin{aligned} f_m^{(3)}(t) = & \sum_{n=1}^5 c_{n,0}\dot{w}_{m,n}^{(3)} + c_{2,1}(\dot{w}_{m+1,2}^{(3)} + \dot{w}_{m-1,2}^{(3)}) \\ & - \sum_{n=1}^5 b_{n,0}w_{m,n}^{(3)} - b_{2,1}(w_{m+1,2}^{(3)} + w_{m-1,2}^{(3)}). \end{aligned} \quad (21)$$

On the top boundary, we take

$$\begin{aligned} \dot{u}_{m,N_y} = & -\sum_{n=2}^5 c_{n,0}\dot{u}_{m,N_y+1-n} - c_{2,1}(\dot{u}_{m+1,N_y-1} + \dot{u}_{m-1,N_y-1}) \\ & + \sum_{n=1}^5 b_{n,0}u_{m,N_y+1-n} + b_{2,1}(u_{m+1,N_y-1} + u_{m-1,N_y-1}) + f_m^{(4)}(t), \end{aligned} \quad (22)$$

$$\begin{aligned}
f_m^{(4)}(t) = & \sum_{n=1}^5 c_{n,0} \dot{w}_{m,N_y+1-n}^{(4)} + c_{2,1} (\dot{w}_{m+1,N_y-1}^{(4)} + \dot{w}_{m-1,N_y-1}^{(4)}) \\
& - \sum_{n=1}^5 b_{n,0} w_{m,N_y+1-n}^{(4)} - b_{2,1} (w_{m+1,N_y-1}^{(4)} + w_{m-1,N_y-1}^{(4)}).
\end{aligned} \tag{23}$$

### 2.3 Heat source via phonon representation

For the entire lattice, a propagating lattice wave is a combination of Fourier modes

$$\begin{aligned}
u_{m,n}^{exact}(t) = & \sum_{p,q} a_{p,q}^{11} \cos(\omega_{p,q}t - \xi_p m - \xi_q n + \phi_{p,q}^{11}) + a_{p,q}^{12} \cos(\omega_{p,q}t - \xi_p m + \xi_q n + \phi_{p,q}^{12}) \\
& + a_{p,q}^{21} \cos(\omega_{p,q}t + \xi_p m - \xi_q n + \phi_{p,q}^{21}) + a_{p,q}^{22} \cos(\omega_{p,q}t + \xi_p m + \xi_q n + \phi_{p,q}^{22}).
\end{aligned} \tag{24}$$

Here the wave vector components  $\xi_p, \xi_q \in [0, \pi]$ , and the corresponding frequency is  $\omega_{p,q} = 2\sqrt{\sin^2(\frac{\xi_p}{2}) + \sin^2(\frac{\xi_q}{2})}$ . The amplitudes  $a_{p,q}^{ij}$  and phases  $\phi_{p,q}^{ij}$  ( $i, j = 1, 2$ ) are specified later.

When restricted to the computational domain with  $N_x \times N_y$  atoms, these waves are maintained under suitable inputs through the boundaries. Noticing the wave propagation direction (Tang and Liu 2015), we take the right-going modes to calculate the source term for the left boundary Eq. (17)

$$w_{m,n}^{(1)}(t) = \sum_{p,q} a_{p,q}^{11} \cos(\omega_{p,q}t - \xi_p m - \xi_q n + \phi_{p,q}^{11}) + a_{p,q}^{12} \cos(\omega_{p,q}t - \xi_p m + \xi_q n + \phi_{p,q}^{12}). \tag{25}$$

In a similar way, we take the left-going modes for the right boundary

$$w_{m,n}^{(2)}(t) = \sum_{p,q} a_{p,q}^{21} \cos(\omega_{p,q}t + \xi_p m - \xi_q n + \phi_{p,q}^{21}) + a_{p,q}^{22} \cos(\omega_{p,q}t + \xi_p m + \xi_q n + \phi_{p,q}^{22}). \tag{26}$$

We take the upward modes for the bottom boundary

$$w_{m,n}^{(3)}(t) = \sum_{p,q} a_{p,q}^{11} \cos(\omega_{p,q}t - \xi_p m - \xi_q n + \phi_{p,q}^{11}) + a_{p,q}^{21} \cos(\omega_{p,q}t + \xi_p m - \xi_q n + \phi_{p,q}^{21}). \tag{27}$$

We take the downward modes for the top boundary

$$w_{m,n}^{(4)}(t) = \sum_{p,q} a_{p,q}^{12} \cos(\omega_{p,q}t - \xi_p m + \xi_q n + \phi_{p,q}^{12}) + a_{p,q}^{22} \cos(\omega_{p,q}t + \xi_p m + \xi_q n + \phi_{p,q}^{22}). \tag{28}$$

Based on a phonon representation for finite temperature lattice motion (Karpov *et al.* 2007, Born 1954), we may confine  $\xi_p, \xi_q \in [\pi/4, 3\pi/4]$ . In numerical implementations, only discrete wave numbers are chosen, at a step size  $\Delta\xi = \frac{\pi}{40}$  for both  $\xi_p$  and  $\xi_q$ . Let  $N_c$  count the number of different modes in the specified interval. The total number of the different modes for each

boundary equals to  $2N_c$ . If the target temperature is  $T$ , we take amplitude  $a_{p,q}^{ij} = \sqrt{\frac{T}{2N_c \omega_{p,q}^2}}$  to realize equal energy distribution among all modes. Furthermore,  $\phi_{p,q}^{ij} \in [0, 2\pi]$  are the random phases.

Our formulation actually allows wave inputs at different temperature for each direction. For instance, if we take  $T_L$  and  $T_R$  for the right-going wave and left-going wave, respectively, the amplitudes are taken as

$$a_{p,q}^{1j} = \sqrt{\frac{T_L}{2N_c \omega_{p,q}^2}}, \quad a_{p,q}^{2j} = \sqrt{\frac{T_R}{2N_c \omega_{p,q}^2}} \quad (29)$$

for  $j=1,2$ .

### 3. Microscopic definitions of thermodynamic quantities

Following (Lepri *et al.* 2003) and (Barik 2006), we define local temperature and heat flux for the square lattice. The local energy contributed by  $(m,n)$  atom is

$$h_{m,n}(t) = \frac{1}{2} \dot{u}_{m,n}^2 + \frac{1}{2} [V(u_{m+1,n} - u_{m,n}) + V(u_{m,n} - u_{m-1,n}) + V(u_{m,n+1} - u_{m,n}) + V(u_{m,n} - u_{m,n-1})]. \quad (30)$$

The first term represents the kinetic energy, while the other terms represent the sum of half the pairwise potential energy.

We define a time-dependent system temperature (average kinetic energy),

$$T(t) = \frac{1}{N_x N_y} \sum_{m=1}^{N_x} \sum_{n=1}^{N_y} \dot{u}_{m,n}^2(t). \quad (31)$$

When local equilibrium is reached, a local temperature may be computed from

$$T_{m,n} = \frac{1}{t - t_c} \int_{t_c}^t \dot{u}_{m,n}^2(\tau) d\tau. \quad (32)$$

Here  $t_c$  is a proper truncation time, and  $t$  is big enough. The local temperature of  $m$ -th layer and  $n$ -th layer are respectively defined as

$$T_m = \frac{1}{N_y} \sum_{n=1}^{N_y} T_{m,n}, \quad T_n = \frac{1}{N_x} \sum_{m=1}^{N_x} T_{m,n}. \quad (33)$$

Substituting the exact lattice motion Eq. (24) with amplitudes specified by Eq. (29) into Eq. (32), we get an exact expression for the local temperature, after some lengthy but straightforward calculations,

$$\begin{aligned}
T_{m,n}^{exact} = & \frac{T_L + T_R}{2} + \frac{1}{2N_c} \sum_{p,q} [T_L \cos(-2\xi_q n + \phi_{p,q}^{11} - \phi_{p,q}^{12}) + \sqrt{T_L T_R} \cos(-2\xi_p m + \phi_{p,q}^{11} - \phi_{p,q}^{21}) \\
& + \sqrt{T_L T_R} \cos(-2\xi_p m - 2\xi_q n + \phi_{p,q}^{11} - \phi_{p,q}^{22}) + \sqrt{T_L T_R} \cos(-2\xi_p m + 2\xi_q n + \phi_{p,q}^{12} - \phi_{p,q}^{21}) \\
& + \sqrt{T_L T_R} \cos(-2\xi_p m + \phi_{p,q}^{12} - \phi_{p,q}^{22}) + T_R \cos(-2\xi_q n + \phi_{p,q}^{21} - \phi_{p,q}^{22})]
\end{aligned} \quad (34)$$

The temperature over the whole lattice is then naturally  $T = \frac{T_L + T_R}{2}$ .

On the other hand, the local energy evolves according to

$$\begin{aligned}
\frac{dh_{m,n}}{dt} = & \frac{1}{2} (u_{m+1,n} - u_{m,n})(\dot{u}_{m+1,n} + \dot{u}_{m,n}) - \frac{1}{2} (u_{m,n} - u_{m-1,n})(\dot{u}_{m,n} + \dot{u}_{m-1,n}) \\
& + \frac{1}{2} (u_{m,n+1} - u_{m,n})(\dot{u}_{m,n+1} + \dot{u}_{m,n}) - \frac{1}{2} (u_{m,n} - u_{m,n-1})(\dot{u}_{m,n} + \dot{u}_{m,n-1}).
\end{aligned} \quad (35)$$

We define a horizontal transient heat flux

$$j_{m,n}^x(t) = \frac{1}{2} [u_{m,n}(t) - u_{m+1,n}(t)] [\dot{u}_{m,n}(t) + \dot{u}_{m+1,n}(t)], \quad (36)$$

which represents the heat flow from  $(m, n)$  atom to  $(m+1, n)$  atom. Similarly, we define the vertical transient heat flux

$$j_{m,n}^y(t) = \frac{1}{2} [u_{m,n}(t) - u_{m,n+1}(t)] [\dot{u}_{m,n}(t) + \dot{u}_{m,n+1}(t)], \quad (37)$$

which represents the heat flow from  $(m, n)$  atom to  $(m, n+1)$  atom.

The heat flux vector is then

$$\vec{j}_{m,n} = (j_{m,n}^x, j_{m,n}^y). \quad (38)$$

A discrete version of its divergence reads

$$\nabla^D \cdot \vec{j}_{m,n} = \frac{j_{m,n}^x - j_{m-1,n}^x}{a} + \frac{j_{m,n}^y - j_{m,n-1}^y}{a}. \quad (39)$$

This gives a conservation law for energy,

$$\dot{h}_{m,n}(t) + \nabla^D \cdot \vec{j}_{m,n} = 0. \quad (40)$$

We further define the time average of heat flux

$$J_{m,n}^x = \frac{1}{t - t_c} \int_{t_c}^t j_{m,n}^x(\tau) d\tau, \quad J_{m,n}^y = \frac{1}{t - t_c} \int_{t_c}^t j_{m,n}^y(\tau) d\tau. \quad (41)$$

According to the exact lattice motion, we can find exact expressions

$$J_{m,n}^{x,exact} = \sum_{p,q} \frac{\sin \xi_p}{2N_c \omega_{p,q}} \left[ (T_L - T_R) + T_L \cos(-2\xi_q n + \phi_{p,q}^{11} - \phi_{p,q}^{12}) - T_R \cos(-2\xi_q n + \phi_{p,q}^{21} - \phi_{p,q}^{22}) \right], \quad (42)$$

and

$$J_{m,n}^{y,exact} = \sum_{p,q} \frac{\sin \xi_q}{2N_c \omega_{p,q}} \left[ \sqrt{T_L T_R} \cos(-2\xi_p m + \phi_{p,q}^{11} - \phi_{p,q}^{21}) - \sqrt{T_L T_R} \cos(-2\xi_p m + \phi_{p,q}^{12} - \phi_{p,q}^{22}) \right]. \quad (43)$$

Finally, we define an integral for the horizontal heat flux of  $m$ -th layer to monitor the heating process more clearly,

$$J_m^x(t) = \int_0^t \frac{1}{N_y} \sum_{n=1}^{N_y} J_{m,n}^x(\tau) d\tau. \quad (44)$$

## 4. Numerical tests

In this section, we first verify reflection suppression effectiveness for the matching boundary conditions. Then we investigate the boundary inputs and the performance of the boundary treatments under such inputs. We perform atomic simulations for thermal fluctuations at finite temperature and analyze the kinetic energy distribution and heat flux. At last, we simulate atomic motion at finite temperature, with a non-thermal part injected upon a thermal equilibrated state.

We take a computational domain with  $N=80 \times 80$  atoms and use the second order Runge-Kutta method at a time step size  $\Delta t=0.01$ . The details of initial value and boundary conditions are specified later on.

### 4.1 Reflection suppression

First, we take a Gaussian hump for initial displacement profile

$$u_{m,n}(0) = 50e^{-r^2/100} \cos \frac{r}{2} \cos \frac{\pi r}{40}, \quad (45)$$

with

$$r^2 = (m-40)^2 + (n-30)^2. \quad (46)$$

The velocity is uniformly zero initially. This gives a symmetric profile centered at the (40,30) atom. The matching boundary conditions are applied to the four boundaries of the computational domain. As shown in Fig. 7, the hump propagates outward. At time  $t=30$ , the wave front reaches the boundaries and then vanishes gradually out of the computational domain without observable reflection. The subsystem reaches equilibrium shortly after  $t=70$ .

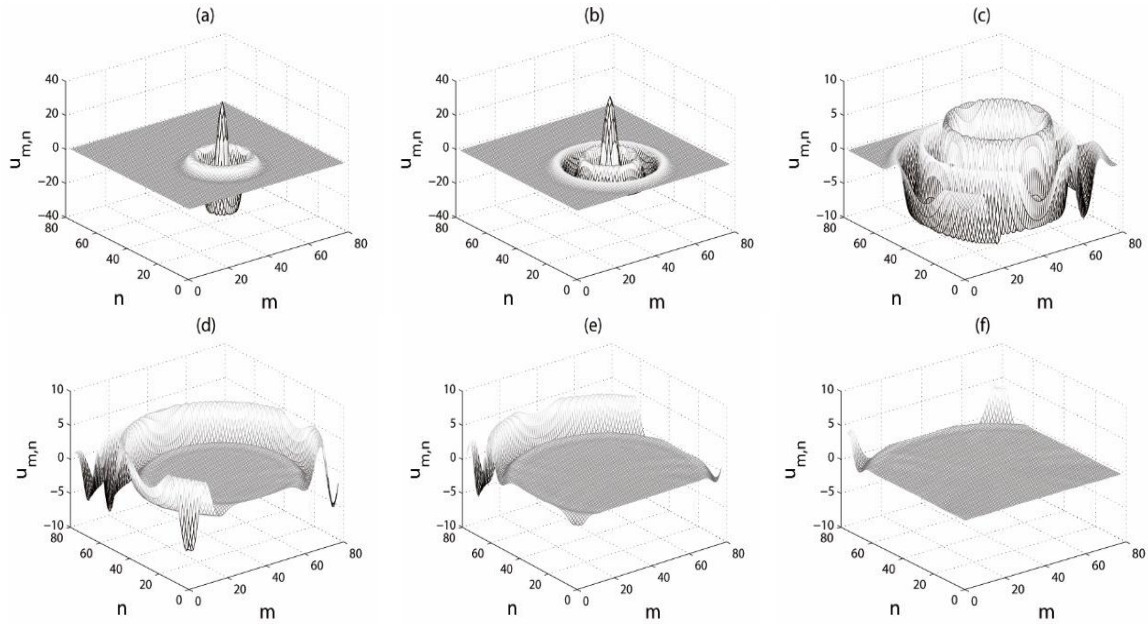


Fig. 7 Propagation of the Gaussian hump: (a)  $u_{m,n}(0)$ ; (b)  $u_{m,n}(10)$ ; (c)  $u_{m,n}(30)$ ; (d)  $u_{m,n}(50)$ ; (e)  $u_{m,n}(60)$ ; (f)  $u_{m,n}(70)$

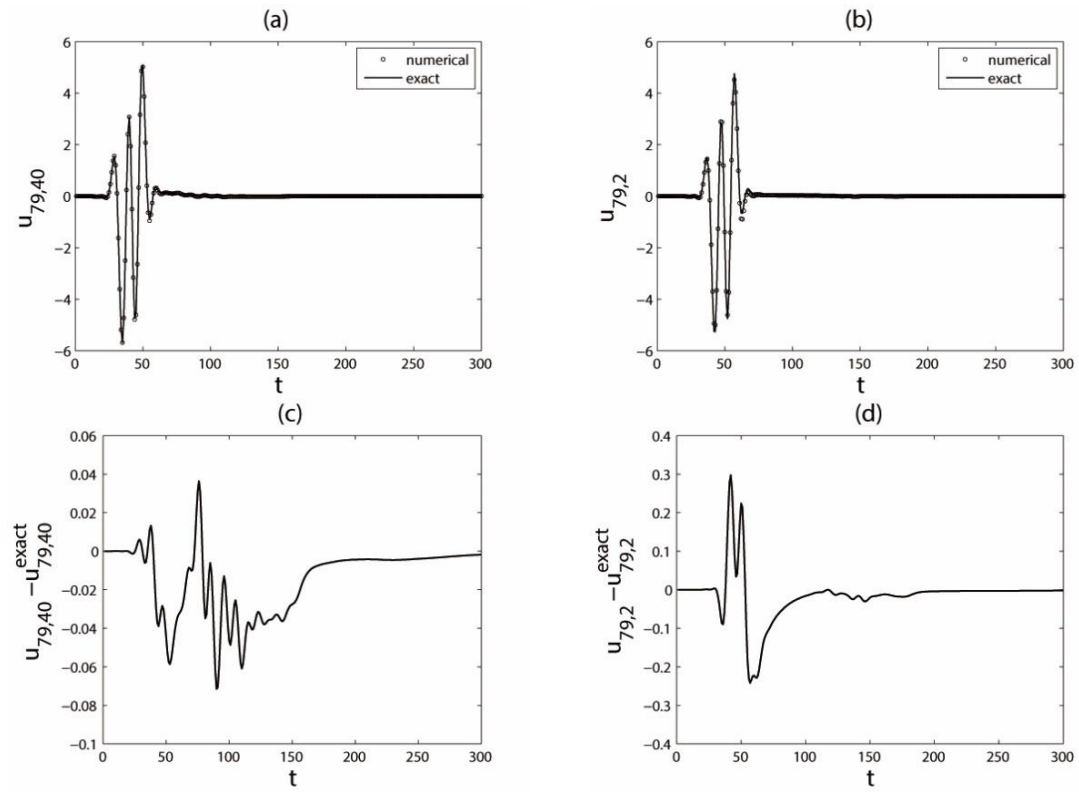


Fig. 8 Gaussian hump: (a)  $u_{79,40}(t)$ ; (b)  $u_{79,2}(t)$ ; (c)  $u_{79,40}^{exact}(t) - u_{79,40}^{numerical}(t)$ ; (d)  $u_{79,2}^{exact}(t) - u_{79,2}^{numerical}(t)$

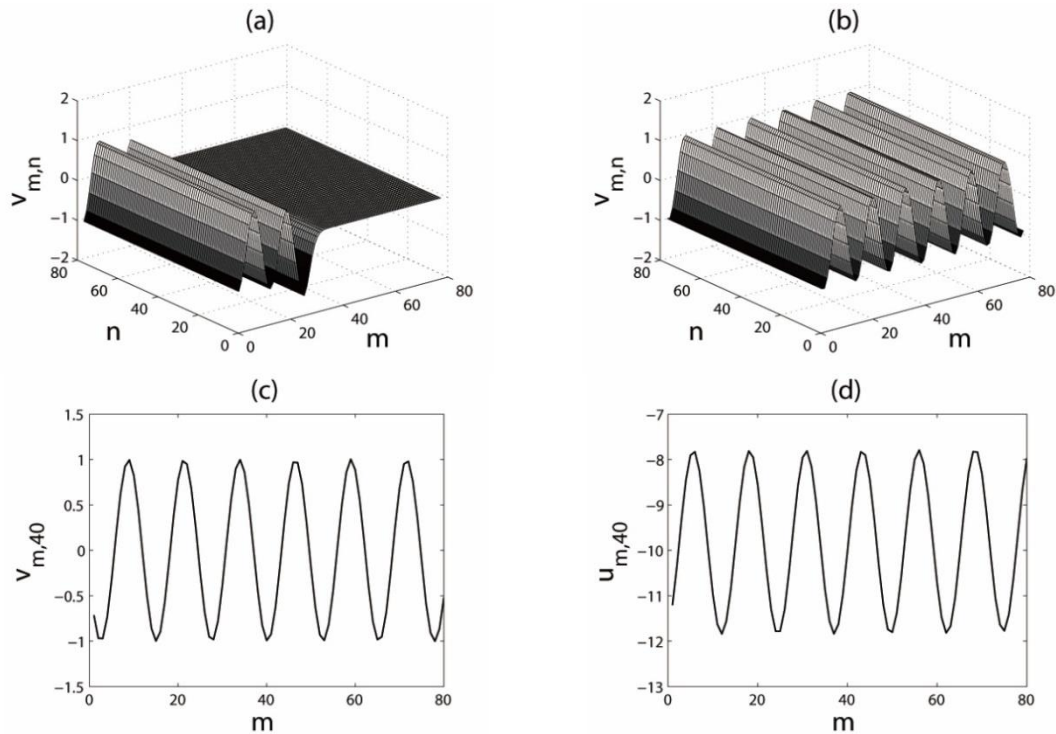


Fig. 9 Normal incident wave from the left boundary: (a)  $v_{m,n}(30)$ ; (b)  $v_{m,n}(120)$ ; (c)  $v_{m,40}(120)$ ; (d)  $u_{m,40}(120)$

To better illustrate the effectiveness, we depict two representative atoms. The (79,40) atom lies at the center of the left boundary. The other atom (79,2) lies at the lower right corner. In Fig. 8, We make a comparison with the reference solution, which is obtained from simulating a system large enough. The wave profiles are basically the same for the two atoms. The hump reaches corner with a delay, as it takes longer time to arrive. In the subplots (a) and (b), we observe that the numerical solution coincides fairly well with the reference solution for both atoms. This demonstrates the accuracy of the proposed boundary treatment. More careful check shows that the discrepancy is bigger for the corner atom in subplot (b), particularly at the peaks. This may be better observed from the difference between the numerical solution and exact solution in subplots (c) and (d). The differences are both quite small, indicating that the matching boundary condition proposed in this work well suppresses reflections. We observe that the difference in  $u_{79,2}(t)$  is bigger than that in  $u_{79,40}(t)$ , which is due to the so-called corner reflections. Corner reflection is a subtle issue, and very expensive to resolve cleanly (Pang and Tang 2011).

#### 4.2 Input through the boundaries

The two-way matching boundary conditions serve for two purposes, namely, to suppress reflections for outgoing waves and to allow injection of incoming ones.

First, we put at the left boundary a monochromatic normal incident wave in the form of  $w_{m,n}^{(l)}(t) = \frac{1}{\omega_{p,q}} \cos(\omega_{p,q}t - \xi_p m)$  with wave vector  $(\xi_p, \xi_q) = (0.5, 0)$ , whereas no input at the right

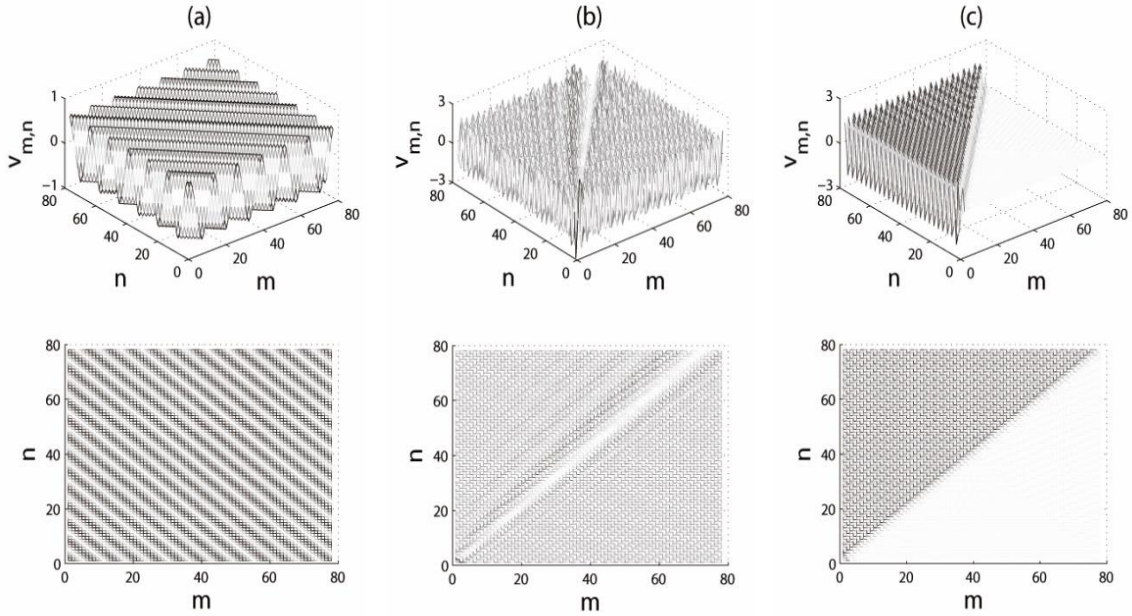


Fig. 10 Oblique incident wave: (a)  $(\xi_p, \xi_q)=(0.5,0.5)$ ,  $\phi_{p,q}^{11} = \phi_{p,q}^{31}$  from the left and bottom boundaries; (b)  $(\xi_p, \xi_q)=(1,2)$ ,  $\phi_{p,q}^{11} \neq \phi_{p,q}^{31}$  from the left and bottom boundaries; (c)  $(\xi_p, \xi_q)=(\frac{\pi}{3}, \frac{2\pi}{3})$  only from the left boundary

boundary. To better clarify the quality for wave injection, we apply periodic boundary conditions at the top and bottom boundaries. All atoms are at equilibrium initially.

As shown in Fig. 9, the monochromatic wave is injected from the left boundary, and propagates toward the right boundary. At  $t=120$ , the wave front has passed through the right boundary without observable reflection. Due to the periodic boundary condition, the square lattice is equivalent to a one-dimensional atomic chain in the horizontal direction. The wave is uniform in the vertical direction. Subplot (c) shows the horizontal velocity profile of the wave, which is sinusoidal. The horizontal displacement profile in subplot (d) shows a displacement drift. We have analyzed it elsewhere and found that the drift is determined by both the initial data and the boundary input. In particular, if initial data is adopted consistent with the input mode as  $u_{m,n}(0) = w_{m,n}^{(1)}(0), \dot{u}_{m,n}(0) = \dot{w}_{m,n}^{(1)}(0)$ , the displacement drift disappears.

Next, we investigate oblique wave injection. Matching boundary conditions are taken at all four boundaries. Let an oblique wave go toward the upper right direction in the infinite lattice. It enters the numerical sublattice only through the left and bottom boundaries. Accordingly, we send a monochromatic wave for these two boundaries in form of  $w_{m,n}^{(1)}(t) = w_{m,n}^{(3)}(t) = \cos(\omega_{p,q}t - \xi_p m - \xi_q n + \phi_{p,q})$ . In subplot (a) of Fig. 10, we display the velocity profile at  $t=3000$  for a numerical example with  $(\xi_p, \xi_q)=(0.5,0.5)$ , both a three-dimensional view (upper row) and a top view (lower row). The wave is successfully injected into the sublattice. The wave propagation direction coincides with the incident angle, which is  $\pi/4$ .

It is worth mentioning that there are two angles related to wave propagation, corresponding to

the phase velocity and the group velocity. The former gives an angle

$$\theta = \arctan \frac{\xi_q}{\xi_p}. \quad (47)$$

On the other hand, the group velocity is

$$\nabla_{(\xi_p, \xi_q)} \omega_{p,q} = \left( \frac{\sin \xi_p}{2\sqrt{\sin^2 \frac{\xi_p}{2} + \sin^2 \frac{\xi_q}{2}}}, \frac{\sin \xi_q}{2\sqrt{\sin^2 \frac{\xi_p}{2} + \sin^2 \frac{\xi_q}{2}}} \right). \quad (48)$$

This gives another angle

$$\eta = \arctan \left( \frac{\sin \xi_q}{\sin \xi_p} \right). \quad (49)$$

For the wave vector  $(\xi_p, \xi_q)=(0.5,0.5)$ , both angles are  $\pi/4$ . To check which of the two angles governs the wave injection, we put along the left boundary  $w_{m,n}^{(1)}(t) = \cos(\omega_{p,q}t - \xi_p m - \xi_q n + \phi_{p,q}^{11})$ , and along the bottom boundary  $w_{m,n}^{(3)}(t) = \cos(\omega_{p,q}t - \xi_p m - \xi_q n + \phi_{p,q}^{31})$ . Now we set the phases different and take  $(\xi_p, \xi_q)=(1,2)$ , for which the angle for phase velocity is  $\theta=1.107$  (close to  $\frac{\pi}{3}$ ),

and that for group velocity is  $\eta=0.824$  (close to  $\frac{\pi}{4}$ ). The resulting wave profile, again at  $t=3000$ , is not a monochromatic one. It is even not a plane wave, a discontinuity appears along the direction of  $\eta$  rather than  $\theta$ , due to the mismatch of the random phase of the incident waves. See subplot (b).

We further check the propagation direction by removing the bottom input, and take  $(\xi_p, \xi_q) = (\frac{\pi}{3}, \frac{2\pi}{3})$ , for which  $\theta$  is again approximately  $\frac{\pi}{3}$  and  $\eta = \frac{\pi}{4}$ . As shown in subplot (c), the wave front clearly lies along the  $\pi/4$  direction.

We conclude that an oblique wave propagates according to the group velocity. Consequently, if the incident wave has a mismatch in phase, namely,  $\phi_{p,q}^{11} \neq \phi_{p,q}^{31}$ , there develops a discontinuity along the direction with the angle  $\eta$ . Consequently, in the heat bath inputs, we cannot arbitrarily assign the amplitudes and random phases for the four boundaries. The amplitudes and the random phases should be consistent for each monochromatic wave mode.

#### 4.3 Heat bath and finite temperature simulations

Now, we are ready to simulate the harmonic square lattice at finite temperature. Matching boundary condition with inputs are applied to the four boundaries. The inputs are in the form of phonon representation described in Section 2. The initial data for the atomic displacement and velocity in the computational subdomain are set to zero.

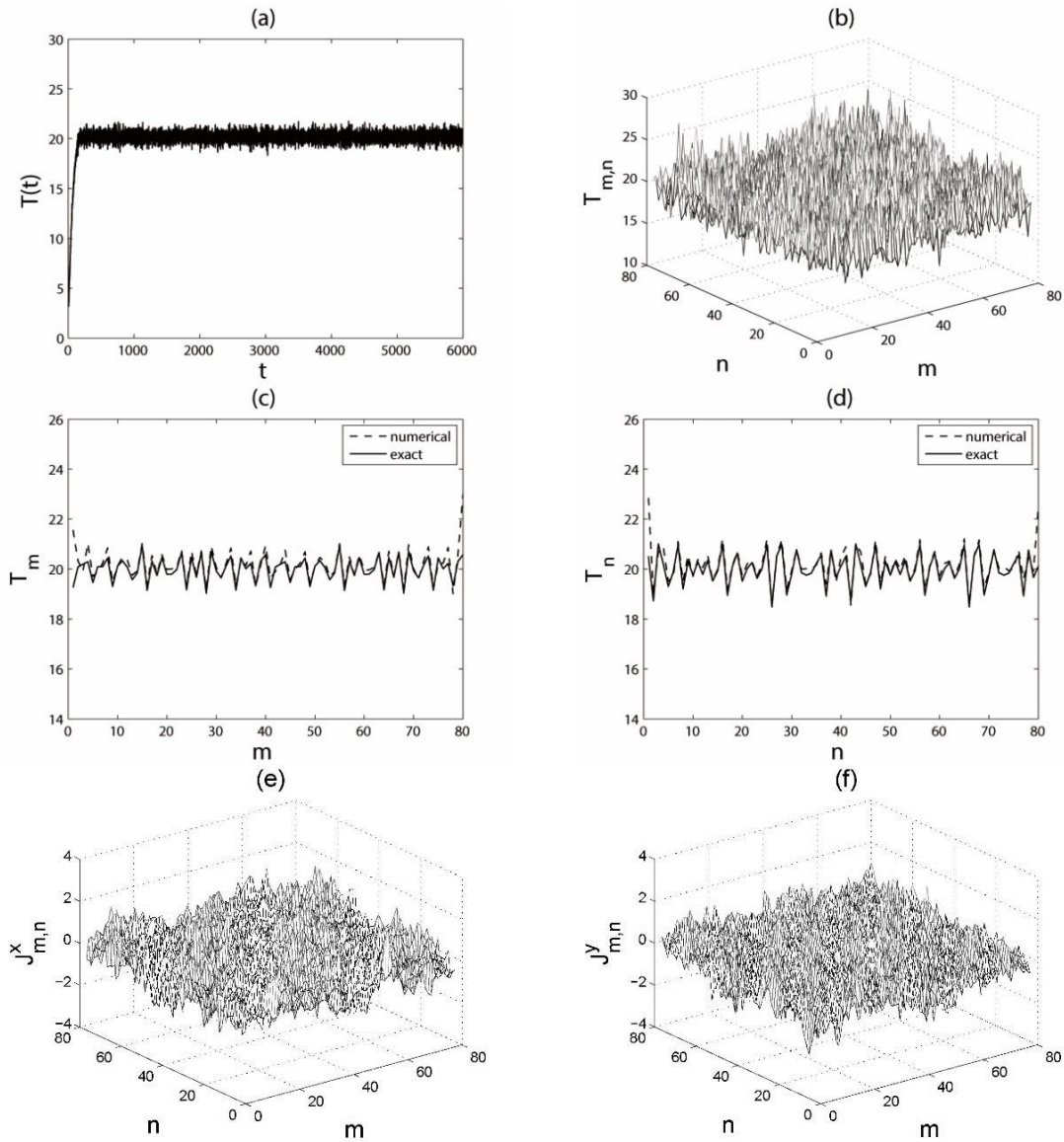


Fig. 11 Heating process for  $T_L=T_R=20$ : (a) system temperature; (b) local temperature; (c)  $m$ -th layer temperature; (d)  $n$ -th layer temperature; (e) horizontal heat flux; (f) vertical heat flux

First, we inject heat jets at temperature  $T_L=T_R=20$ . As shown in subplot (a) of Fig. 11, the system temperature  $T(t)$  rises up to the target temperature  $T_0=20$  as expected, at a time about  $t=100$ . This corresponds to the time for injected waves propagating to the other side of the subdomain. At thermal equilibrium, the local temperature  $T_{m,n}$  fluctuates around the target temperature. See subplot (b). The  $m$ -th layer temperature  $T_m$  and the  $n$ -th layer temperature  $T_n$  are displayed in subplots (c) and (d). Comparison with the exact profile given by Eq. (34) exposes good agreement between the numerical result and the exact profile. The computed temperatures are slightly higher near the boundaries. This is due to long time integration, as well as minor yet

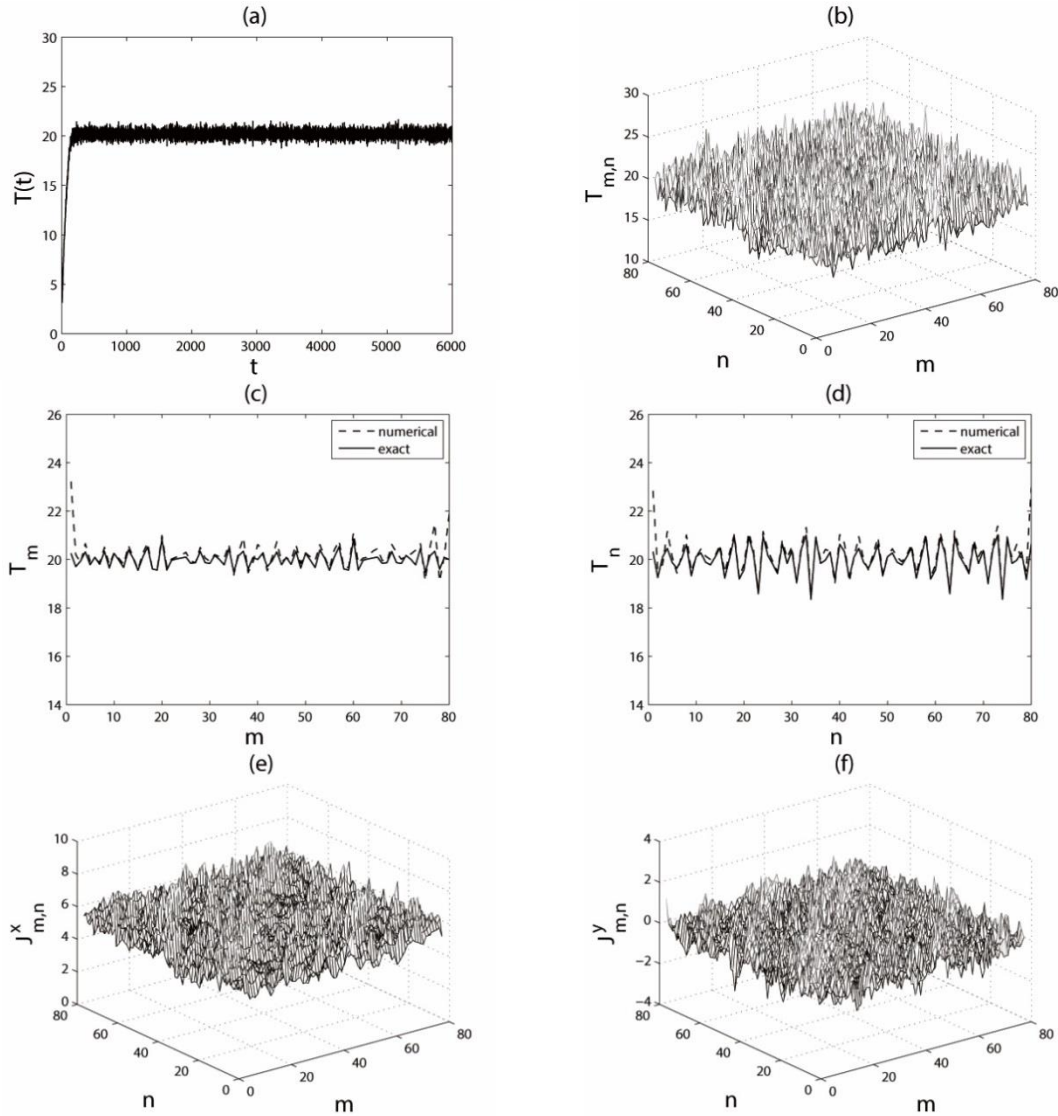


Fig. 12 Heating process for  $T_L=32$ ,  $T_R=8$ : (a) system temperature; (b) local temperature; (c)  $m$ -th layer temperature; (d)  $n$ -th layer temperature; (e) horizontal heat flux; (f) vertical heat flux

existing numerical reflections. In subplots (e) and (f), the time-average of horizontal heat flux  $J^x_{m,n}$  and vertical heat flux  $J^y_{m,n}$  fluctuate around zero, indicating that thermal equilibrium is reached.

Next, we inject heat jets at different temperatures  $T_L=32$  and  $T_R=8$ . In subplot (a) of Fig. 12, the system is again heated to the target temperature  $T_0=20$ . The heating process and the local temperature are similar to the previous case. However, in subplot (e), the horizontal heat flux  $J^x_{m,n}$  fluctuates around a certain value, higher than the previous case. Actually this mean value of  $J^x_{m,n}$  is approximately 5.57, consistent with the exact expression Eq. (42). On the other hand, the

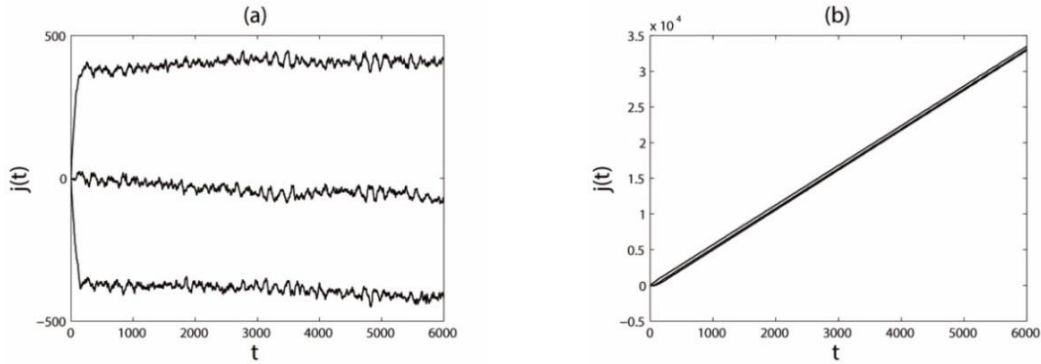


Fig. 13 The integrals of the horizontal heat flux  $J_3^x(t)$ ,  $J_{40}^x(t)$  and  $J_{77}^x(t)$  with temperature of inputs: (a)  $T_L=T_R=20$ ; (b)  $T_L=32, T_R=8$

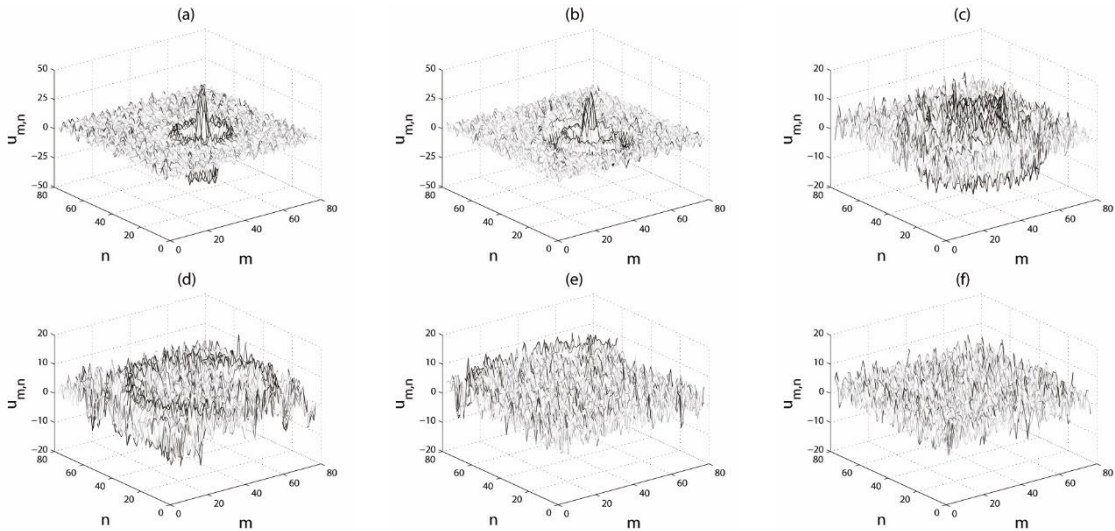


Fig. 14 Atomic simulation of a Gaussian hump at finite temperature by the heat jet approach: (a)  $u_{m,n}(2000)$ ; (b)  $u_{m,n}(2010)$ ; (c)  $u_{m,n}(2020)$ ; (d)  $u_{m,n}(2040)$ ; (e)  $u_{m,n}(2060)$ ; (f)  $u_{m,n}(2100)$

vertical heat flux  $J_{m,n}^y$  still fluctuates around zero in subplot (f). The difference in the heat flux reveals a net heat flow from left side to right side. Moreover, as seen from subplot (c), no horizontal temperature gradient is established when different temperatures are applied to the two sides, because no phonon scattering exists in the harmonic lattice.

As calculated before, the lattice target temperature is the mean of the heat jet temperatures at the two sides, namely equals to  $\frac{T_L + T_R}{2}$ . The temperature profiles distribute randomly for each run due to the random heat sources. The fluctuations in the system temperature and the local temperature decrease when more normal modes are included in general.

We further display the integrals of the horizontal heat flux in Fig. 13. In subplot (a) for the same temperature at two sides,  $j_3^x(t)$  rises up to about 400, and  $j_{77}^x(t)$  decreases to about -400.

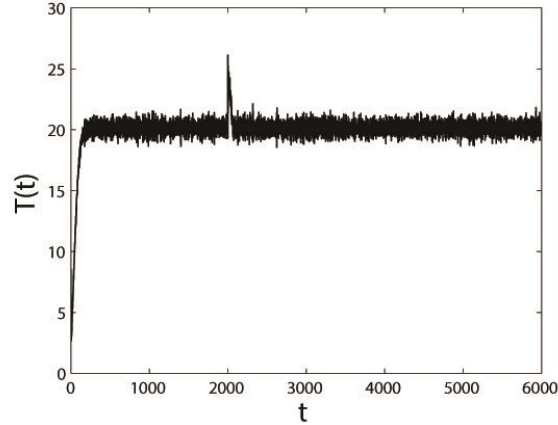


Fig. 15 Nominal system temperature in finite temperature atomic simulation with  $T_L=T_R=20$

This shows a thermal flow. When the steady state is established, the heat flux integrals  $j_3^x(t)$ ,  $j_{40}^x(t)$  and  $j_{77}^x(t)$  oscillate around a certain level. In contrast, when the temperatures are different at two sides, the integral curves in subplot (b) rise indefinitely. They have the same slope, corresponding to the average of  $J_{m,n}^x$  in Fig. 12(e).

Finally, we illustrate a finite temperature atomic simulation. Adding the Gaussian hump Eq. (45) at  $t=2000$  upon a thermal equilibrated state with  $T_L=T_R=20$ , we simulate the evolution of the non-thermal motion in the lattice at finite temperature.

In Fig. 14, the Gaussian hump spreads on top of the thermal fluctuations, and propagates gradually outward. At  $t=2020$ , the hump reaches the boundaries and further goes out, until vanishes at  $t=2100$ . The amplitude of the Gaussian hump is bigger than the thermal fluctuations initially. So the nominal system temperature goes up sharply when it is added at  $t=2000$ . See Fig. 15. Along with the Gaussian hump propagation, the nominal system temperature decreases quickly. When the hump completely leaves the lattice, the nominal system temperature returns back to the target temperature.

## 5. Summary

In this paper, we formulate a heat jet approach to realize a linear thermostat for the out-of-plane motion of a square harmonic lattice. It is based on a two-way matching boundary condition, which is designed by matching the dispersion relation at long wave limit as well as a set of selected wave vectors. We perform a reflection coefficient analysis and numerical tests to demonstrate the effectiveness of this boundary treatment for reflection suppression. This guarantees the computational sublattice correctly recover the physics of the entire lattice if waves propagate outward only. In addition, with a source term designed by the two-way boundary condition and a given incoming wave, the boundary treatment allows full injection without numerical artifact. This is demonstrated by a numerical example of an incident plane wave. Analytical proof is similar to the one dimensional case (Tang and Liu 2015), which we omit here. We further explore the

manner for setting up source terms from the four boundaries of a rectangular sublattice. Waves actually propagate along a direction dictated by the group velocity, instead of by the phase velocity. If the phases or the amplitudes for different boundaries are not in full agreement, numerical discontinuities appear. This understanding guides us to design numerical sources appropriate for the phonon representation of thermal fluctuations. As everything is linear in the proposed approach, we readily obtain explicit expressions for the dynamics of the atomic motions and accordingly those for the thermodynamic quantities. Numerical tests verify these expressions. In particular, the sublattice temperature at thermal equilibrium is the mean of the boundary input temperatures. Numerical tests illustrate the atomic motions and thermodynamic process.

With all these preparatory works done, finite temperature atomic computations are performed. Stemmed from the linear nature of the governing system and the algorithm, the proposed heat jet approach precisely reproduces a superposition of wave propagation for the non-thermal part and thermal fluctuations, without overestimation of the system temperature or the over-damping of the non-thermal motion. Therefore, the designed boundary treatment fulfills the goal of reproduce faithfully the numerics of the entire lattice, at the cost of computing a small subsystem.

As we have demonstrated for one dimensional chains, the heat jet approach for the square lattice applies to moderately nonlinear systems at a temperature not very high. Furthermore, it provides a key component in accurate finite temperature multiscale computations, under a suitable framework such as finite difference multiscale approach (Tang 2008, Tang *et al.* Preprint). Our approach, as it is clear and linear, may provide a new reliable numerical platform for the study of thermal conduction problems.

We remark that a vital component in the proposed heat jet approach is the design of an effective boundary condition. This is highly nontrivial for each crystalline structure and potential. Furthermore, in high space dimensions, the phonon representation involves enormous summations, and induces heavy computing costs. Reasonable yet physically meaningful simplifications are desirable.

## Acknowledgments

This research is partially supported by NSFC under grant No. 11272009 and 11521202. We would like to thank Professor Hong Zhao and the anonymous referee for stimulating discussions.

## References

- Ai, B. and Hu, B. (2011), "Heat conduction in deformable frenkel-kontorova lattices: Thermal conductivity and negative differential thermal resistance", *Phys. Rev. E.*, **83**(1), 011131.
- Andersen, H.C. (1980), "Molecular dynamics simulations at constant pressure and/or temperature", *J. Chem. Phys.*, **72**(4), 2384-2393.
- Barik, D. (2006), "Heat conduction in 2D harmonic lattices with on-site potential", *Europhys. Lett.*, **75**(1), 42-48.
- Berendsen, H.J., Postma, J.V., Van Gunsteren, W.F., DiNola, A.R.H.J. and Haak, J.R. (1984), "Molecular dynamics with coupling to an external bath", *J. Chem. Phys.*, **81**(8), 3684-3690.
- Born, M. and Huang, K. (1954), *Dynamical Theory of Crystal Lattices*, Clarendon, Oxford.
- Bussi, G. and Parrinello, M. (2007), "Accurate sampling using Langevin dynamics", *Phys. Rev. E.*, **75**(5), 056707.

- Dhar, A. (2008), "Heat transport in low-dimensional systems", *Adv. Phys.*, **57**(5), 457-537.
- Dhar, A., Venkateshan, K. and Lebowitz, J.L. (2011), "Heat conduction in disordered harmonic lattices with energy-conserving noise", *Phys. Rev. E.*, **83**(2), 021108.
- Giardinà, C., Livi, R., Politi, A. and Vassalli, M. (2000), "Finite thermal conductivity in 1D lattices", *Phys. Rev. L.*, **84**(10), 2144-2147.
- Hatano, T. (1999), "Heat conduction in the diatomic Toda lattice revisited", *Phys. Rev. E.*, **59**(1), R1-R4.
- Hoover, W.G. (1985), "Canonical dynamics: Equilibrium phase-space distributions", *Phys. Rev. A.*, **31**(3), 1695-1697.
- Jackson, E.A. and Mistriotis, A.D. (1989), "Thermal conductivity of one-and two-dimensional lattices", *J. Phys. Condens. Matt.*, **1**(7), 1223-1238.
- Karpov, E.G., Park, H.S. and Liu, W.K. (2007), "A phonon heat bath approach for the atomistic and multiscale simulation of solids", *Int. J. Numer. Meth. Eng.*, **70**(3), 351-378.
- Lepri, S., Livi, R. and Politi, A. (2003), "Thermal conduction in classical low-dimensional lattices", *Phys. Rep.*, **377**(1), 1-80.
- Lippi, A. and Livi, R. (2000), "Heat conduction in two-dimensional nonlinear lattices", *J. Stat. Phys.*, **100**(5), 1147-1172.
- Nishiguchi, N., Kawada, Y. and Sakuma, T. (1992), "Thermal conductivity in two-dimensional monatomic non-linear lattices", *J. Phys. Condens. Matt.*, **4**(50), 10227-10236.
- Nosé, S. (1984), "A unified formulation of the constant temperature molecular dynamics methods", *J. Chem. Phys.*, **81**(1), 511-519.
- Pang, G. and Tang, S. (2011), "Time history kernel functions for square lattice", *Comput. Mech.*, **48**(6), 699-711.
- Savin, A.V. and Kosevich, Y.A. (2014), "Thermal conductivity of molecular chains with asymmetric potentials of pair interactions", *Phys. Rev. E.*, **89**(3), 032102.
- Tang, S. (2008), "A finite difference approach with velocity interfacial conditions for multiscale computations of crystalline solids", *J. Comput. Phys.*, **227**(8), 4038-4062.
- Tang, S. (2010), "A two-way interfacial condition for lattice simulations", *Adv. Appl. Math. Mech.*, **2**, 45-55.
- Tang, S. and Liu, B. (2015), "Heat jet approach for atomic simulations at finite temperature", *Comm. Comput. Phys.*, **18**(5), 1445-1460.
- Tang, S., Zhang, L., Ying, Y.P. and Zhang, Y.J. "A finite difference approach for finite temperature multiscale computations", Preprint.
- Wang, X. and Tang, S. (2013), "Matching boundary conditions for lattice dynamics", *Int. J. Numer. Meth. Eng.*, **93**(12), 1255-1285.
- Xiong, D., Wang, J., Zhang, Y. and Zhao, H. (2010), "Heat conduction in two-dimensional disk models", *Phys. Rev. E.*, **82**(3), 030101.
- Xiong, D., Zhang, Y. and Zhao, H. (2014), "Temperature dependence of heat conduction in the fermi-pastulam-beta lattice with next-nearest-neighbor coupling", *Phys. Rev. E.*, **90**(2), 022117.
- Yang, L. (2002), "Finite heat conduction in a 2D disorder lattice", *Phys. Rev. Lett.*, **88**(9), 094301.
- Yang, L., Grassberger, P. and Hu, B. (2006), "Dimensional crossover of heat conduction in low dimensions", *Phys. Rev. E.*, **74**(6), 062101.
- Zhong, Y., Zhang, Y., Wang, J. and Zhao, H. (2012), "Normal heat conduction in one-dimensional momentum conserving lattices with asymmetric interactions", *Phys. Rev. E.*, **85**(6), 060102.